Large-Eddy simulation of the airflow around a truck

Patel, Nainesh; He, Mingzhe; Hemida, Hassan; Quinn, Andrew

[Link to publication on Research at Birmingham portal](#)

1   **Large-Eddy Simulation of the Airflow Around a Truck**

2   Nainesh Patel, Mingzhe He*, Hassan Hemida, Andrew Quinn

3   *School of Civil Engineering, University of Birmingham, B15 2TT, UK.

4   Corresponding author: m.he@bham.ac.uk

5   **Abstract**

6   Understanding the complex and unsteady flow around commercial vehicles is crucial for
7   improving the aerodynamic performance and safety. Large-Eddy Simulation (LES) is an
8   excellent tool for understanding and visualising the flow structures, which is normally difficult
9   to achieve in experiments. This paper examines a 1:25 scale model truck subjected to a
10   headwind. Both LES and Reynolds-Averaged Navier-Stokes (RANS) techniques were used to
11   acquire the aerodynamic coefficients and surface pressure. Pressure coefficients from LES
12   show good agreement with the full-scale data while discrepancies were found for RANS. The
13   complex flow structures around the truck are presented in detail through streamlines, isosurface
14   contours and surface trace lines, based on the LES results. Both time-averaged and
15   instantaneous vortex structures are identified, highlighting the highly turbulent regions with
16   high energy dissipations, as well as the propagation of small vortices along the truck surface.
17   Spectral analysis is carried out on the time-varying aerodynamic coefficients, showing the
18   dominant frequencies in vortex shedding. Two potential instability modes were identified
19   corresponding to large-scale vortex shedding at low Strouhal number and small-scale vortex
20   shedding due to Kelvin Helmholtz instability. The outcome of the work will help the designers
21   and manufacturers improve the aerodynamic performance and safety of commercial trucks.

22   **1.   Introduction**

23   The airflow around a ground vehicle is characterised by fluctuating velocities and pressures in
24   both space and time. Understanding of the aerodynamics of the vehicles is of great significance
25   not only because the aerodynamic performance is directly related to fuel consumption and
26   environmental impact but also the wind-induced accidents may result in loss of lives and
27   property. Full-scale and wind tunnel experiments are the common methods for investigating
28   vehicle aerodynamics (Coleman and Baker, 1994, Coleman and Baker, 1990, Baker, 1991b,
29   Baker, 1991a, Quinn et al., 2007, Cheli et al., 2011). A common objective in these studies is to
30   investigate the time-averaged aerodynamic forces and moments, whereas it is usually difficult
31   to get a clear perspective of the flow structures, which plays a pivotal role in improving the
32   resilience of vehicle design. Therefore, there has been growing interest in using CFD to
33   supplement the experiments. Both are vital to get a full picture of the aerodynamics of vehicles.

34   Among all types of ground vehicles, the commercial vehicles, i.e. trucks, are responsible for a
35   large proportion of the greenhouse gas emission, according to the Department of Transport
36   (2015). More importantly, these high-sided vehicles are usually susceptible to wind-induced
37   instabilities (Cheli et al., 2006, Cheli et al., 2011, Quinn et al., 2007). As part of an EU funded
38   project (WEATHER), Cheli et al. (2006) conducted wind tunnel test on a truck model and
39   developed an experimental-numerical approach to evaluate the wind loading on trucks under
40   given turbulent wind conditions. In the meanwhile, full-scale experiments on the same truck
41   were carried out by Quinn et al. (2007). Rolling moments were measured and the pressure was
42   captured for a number of positions on the truck container box. The same problem was
43   numerically examined by Hargreaves and Moran (2007) who used the unsteady RANS
44   (URANS) approach, with the aim to verify the applicability of this approach for this type of
45   highly unsteady problem. The URANS results showed good agreement with the full-scale and
46   wind tunnel data regarding the rolling moment coefficients but this approach failed to predict
47   the flow separation on the roof. Therefore, other techniques such as Detached Eddy Simulation
48   (DES) or even LES were recommended the authors for future investigations.

The work carried out by Cheli et al. (2006), Quinn et al. (2007) and Hargreaves and Morvan (2007) focused on finding the aerodynamic forces and moments. However, the flow structures around the truck are still unknown. To the authors' knowledge, there is no such research on this type of truck. For other vehicle shapes, some researchers have used Detached Eddy Simulations (DES) to understand the flow field around ground vehicles, which provide promising results (Hemida and Krajnović, 2009, Diedrichs, 2010, Guilmineau et al., 2011, Hyams et al., 2011). This method is more computationally intensive than RANS since large-scale flow structures are resolved in the far-field region away from the boundaries. However, close to the boundaries, the flow is not resolved but instead, modelled through a RANS approach. Therefore, DES may sometimes underestimate the flow separation and it is challenging to deal with the "grey area", where it switches from RANS to LES or vice versa (Spalart, 2009). As a result, a more accurate method, i.e. LES, has been employed by a number of researchers to investigate the wind behaviour around bluff bodies (Krajnović and Davidson, 2002b, Krajnović and Davidson, 2005b, Krajnović and Davidson, 2005a, Krajnović, 2009, Hemida and Baker, 2010, Hemida and Krajnović, 2010, Krajnović and Fernandes, 2011). LES is of course computationally more expensive than RANS and DES. However, it fundamentally produces more accurate instantaneous and time-averaged results, since LES resolves all the large-scale flow structures down to the wall and only the smallest scales are modelled.

The aim of the work presented in this paper is, therefore, to investigate the flow behaviour around a truck using LES. It is of interest to obtain time-dependent as well as time-averaged flow in order to gain an understanding of the relationship between the flow structures around the truck and the corresponding aerodynamic forces acting upon it. Additionally, force spectra are investigated to identify the vortex shedding frequencies.

Initially in this paper, the physical truck model of interest is introduced in section 2, followed by a detailed description of the methods used. These include the numerical method, the computational domain, boundary conditions, mesh generation and discretisation schemes. Surface pressure from the simulations is validated against the experimental data, as shown in section 4. The time-averaged aerodynamic forces and moments coefficients obtained from both LES and RANS are presented in the following section. Section 6 presents detailed investigation and visualisation of the flow structures around the truck via surface trace lines, isosurface contours and streamlines of either slipstream velocities or pressure coefficients. Spectral analysis is carried out on the time-varying coefficients in section 7. The paper ends with the key conclusions and the significance of the work.

2. Truck model

The vehicle investigated herein is in keeping with the one that was previously studied by Quinn et al. (2007) via full-scale measuring. In that study, data was collected on a Leyland DAF 45 truck, which is shown in Fig 1. The Reynolds number in the experimental tests was carried out between 1.2 million and 2.8 million. Performing LES at these Re is not currently feasible, as the mesh required for the full-scale geometry would exceed the available resources. To account for this, a 1:25 scale model representation was used, reducing the Reynolds number to 200,000 based on the free stream velocity and the height of the vehicle. It is acknowledged that there is always to some extent a difference between model-scale and full-scale results due to the disparity in Re. However, Re~10^5 has widely been regarded as a high enough value in which case the aerodynamic coefficients would be similar to those expected at full-scale, or at least the trend should be the same (Hong et al., 1998, Krajnović and Davidson, 2003, Hargreaves and Morvan, 2007, Gallagher et al., 2018, Krajnović and Davidson, 2005b). Indeed, there is limited research available and therefore the Re effects are not conclusive, which requires more systematic study in the future. Figure 1b shows the model representation that was used and Fig. 1c shows that a level of complexity has been maintained in the underbody of the computational model through including the chassis, wheels, mudguards, gearbox and transmission shaft. However, smaller features, such as the glass windows and lights, have not been included. The

1 wheels have a diameter of 29mm and 1.2mm has been cut from the bottom of the wheels to
2 represent the interaction between the tyres and the ground. The truck model that has been used
3 in this study is the same truck that was used by Hargreaves and Morvan (2007). All dimensions
4 in the rest of this paper have been non-dimensionalised with respect to the dimensions of the
5 vehicle, i.e. the height h=0.1398m, the length l=0.3236m and the width w=0.1m. Velocities
6 have been non-dimensionalised with respect to the free stream velocity.
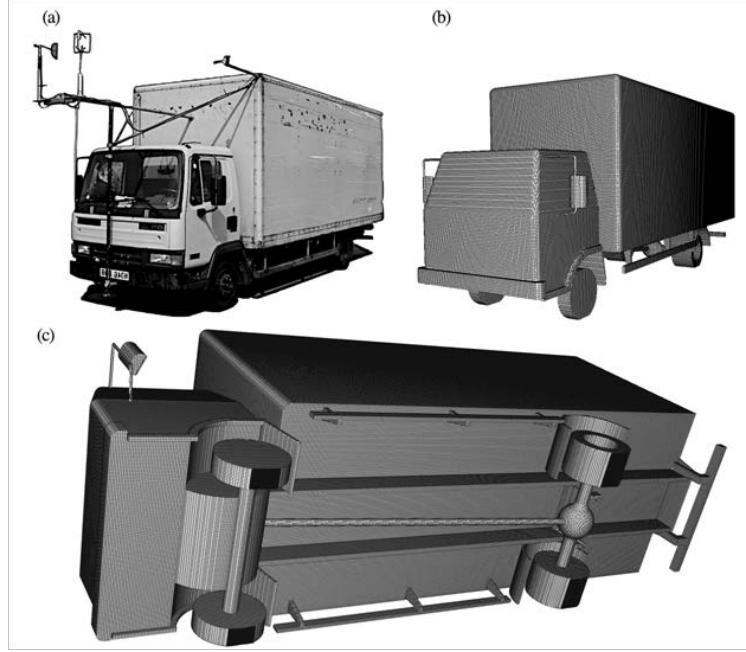
7

8   Fig. 1 (a) Leyland DAF 45 Truck. (b) Computational model of the truck (c) Underbody geometry.

9 **3. Computational methodology**
10   **3.1. Governing equations of LES**

11 Airflow past any bluff body is highly chaotic and is characterised by unsteady fluid flow
12 behaviour, which creates 3-dimensional fluid structures at a range of turbulent length and time
13 scales. The largest structures generally contain the most energy and thus a method that is
14 capable of resolving instantaneous coherent structures is required. A computational method that
15 is suitable for this purpose is Large-Eddy Simulation (LES). In the literature, there is good
16 evidence that demonstrates the successful use of LES to understand the fluid flow behaviour
17 around bluff bodies and vehicles. (Krajnović and Davidson, 2003, Krajnović and Davidson,
18 2005b, Krajnović and Davidson, 2005a, Hemida and Krajnović, 2010, Krajnović et al., 2012).
19 LES decomposes the structure of the flow into large and small scales by a process of filtering
20 which has an associated filter width, Δ. This allows the structures that are generated at the Grid
21 Scale (GS) or larger than the GS to be resolved and scales smaller than Δ require modelling by
22 some sub-grid scale (SGS) models. In LES any flow variable, ϕ, can be decomposed into a
23 resolved component and an SGS component:

24 $$\phi = \bar{\phi} + \phi', \tag{1}$$

25 where ϕ is the instantaneous flow variable, $\bar{\phi}$ is the filtered resolved part, and ϕ' is a residual.
26 To obtain the filtered component, spatial filtering is applied to the instantaneous flow variable
27 using:

28 $$\bar{\phi}(x_i, t) = \int_\Omega G(x_i, x_i'; \Delta)\phi(x_i', t)dx_i' , \tag{2}$$

29 where G is the filter function that determines whether the flow variable is large or not. The
30 incompressible momentum and continuity equations are filtered using an implicit top-hat filter:

31 $$G(x_i, x_i'; \Delta) = \begin{cases} \frac{1}{\Delta} & , \quad \text{if } |x_i - x_i'| < \frac{\Delta}{2} , \\ 0 & , \quad \quad \text{otherwise} \end{cases} \tag{3}$$

32 where Δ is the filter width. In the present simulations, the filter width is taken as the cubic root

of the volume of the cell, $\Delta = \left(\Delta_x\Delta_y\Delta_z\right)^{1/3}$, where Δ_i is the cell size in each respective direction. Hence the filtered incompressible momentum equations and continuity equation are given by:

$$\bar{u}_{i,t} + \left(\bar{u}_i\bar{u}_j\right)_{,j} = -\frac{1}{\rho}\bar{p}_{,i} + \nu\bar{u}_{i,jj} - \tau_{ij,j}, \tag{4}$$

$$\bar{u}_{i,i} = 0, \tag{5}$$

where $\bar{u}_i$ and $\bar{p}$ is the filtered velocity and pressure respectively and $\tau_{ij} = \overline{u_i u_j} - \bar{u}_i\bar{u}_j$ are the SGS stresses. It should be noted that grid spacing in the mesh is not uniform so a commutation error exists. However, Ghosal and Moin (1995) showed that the commutation errors are of second order in the filter width, $\mathcal{O}(\Delta^2)$. So the induced errors are no larger than the errors introduced by the second order finite difference schemes used in the simulations. In this investigation, the SGS have been modelled using a standard Smagorinsky model (Smagorinsky, 1963). This model is chosen for its straightforwardness and it is free from unnecessary complexities that add to the computational cost. The SGS models the stresses as:

$$\tau_{ij} - \frac{1}{3}\delta_{ij}\tau_{kk} = -2\nu_{SGS}S_{ij}, \tag{6}$$

where S_{ij} is the strain rate tensor, defined by:

$$S_{ij} = \frac{1}{2}\left(\bar{u}_{i,j} + \bar{u}_{j,i}\right), \tag{7}$$

and ν_{sgs} is the SGS viscosity:

$$\nu_{SGS} = (C_s f_{vD}\Delta)^2\left(2S_{ij}S_{ij}\right)^{1/2}. \tag{8}$$

where C_s is the Smagorinsky constant. The open source software package OpenFOAM was used to pre-process the simulations. The implementation of the Smagorinsky coefficient was written in terms of two other parameters c_k and c_e, which represent the level of turbulent kinetic energy and turbulent dissipation, respectively. Thus, the Smagorinsky coefficient is expressed by $C_s = \left(c_k\left(\frac{c_k}{c_e}\right)^{\frac{1}{2}}\right)^{\frac{1}{2}}$. C_s is conventionally taken to be 0.1. In this model, the turbulent kinetic energy was taken to be 0.094 and the turbulent dissipation was taken to be 1.048, which leads to the Smagorinsky coefficient of 0.167. The use of a larger Smagorinsky coefficient implies that the results are over dampened. However, Krajnović and Davidson (2002a) showed that this number has little influence on the simulation. f_{vD} is the van Driest dampening function used to dampen the eddy viscosity close to the wall and is defined by:

$$f_{vD} = 1 - \exp\left(\frac{-y^+}{26}\right). \tag{9}$$

where $y^+ = u_\tau y/\nu$ is the normalised wall distance with u_τ being the friction related velocity and y being the distance to the wall. Whilst other similar formulations of the van Driest damping function exists, this one is commonly used (Inagaki et al., 2005) and has been used in a number of similar studies (Hemida and Baker, 2010, Krajnović et al., 2011).

It is worth mentioning that RANS is also employed in the present work, although the focus is the LES results. RANS approach is fundamentally less favourable for the herein highly unsteady problem. The fact that RANS models all the turbulence via a theoretical model leads to much reduced time to obtain the solution but at the same time, much less accuracy compared to LES. In addition, the Reynolds-averaged approach can only provide time-averaged results and usually suffers from difficulty in solution convergence for highly unsteady problems. Nonetheless, in order to test the accuracy of RANS approach for this type of problem, RANS simulations with two commonly used turbulence models, namely the realizable k-ϵ model and the Shear Stress Transport (SST) k-ω model have been conducted.

3.2. Computational domain and boundary conditions

The truck is placed on the ground in the computational domain, as shown in Fig. 2. Taking h to be the height of the truck from the ground, the domain is 29.6h long, 7.3h high and 10.7h wide.

4

1 The front of the truck has been positioned 8.2h from the inlet and the back of the truck 19.1h
2 from the outlet. These dimensions ensure that the blockage ratio is below 1%. Moreover, the
3 size of the current computational domain is considered to be sufficient in previous LES
4 simulations (Krajnović and Davidson, 2003, Hemida and Baker, 2010, Krajnović et al., 2012).

5 In this study, fluid enters the computational domain with a uniform velocity from the inlet. No-
6 slip boundary conditions have been applied to the surface of the truck and the ground; hence a
7 zero pressure gradient exists at the walls. Slip boundary conditions have been applied to the
8 upper and sidewalls and a convective boundary condition has been used at the outlet. For the
9 RANS simulations, standard wall functions were used for the turbulent kinetic energy,
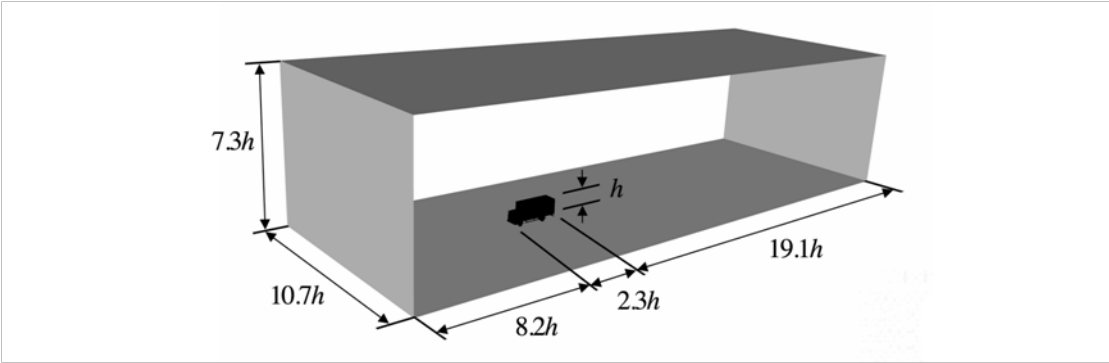10 dissipation and eddy viscosity.

11
12   Fig. 2 Computational domain.

3.3. Mesh

14 The snappyHexMesh utility implemented in OpenFOAM was used to generate the mesh. Two
15 different meshes were generated, a coarse mesh containing 2.8×10^6 cells and a fine mesh
16 containing 11×10^6 cells. The additional 8.2×10^6 cells were defined in the wake and in the
17 boundary layer of the truck. The mesh has been generated primarily with structured hexahedral
18 cells. However, due to the complicated geometry, there also exists a small number of
19 unstructured prisms and polyhedral cells. Fig. 3a shows the boundary layers in the fine mesh
20 on a plane cutting through the centre of the truck. Fig. 3b shows the surface mesh underneath
21 the vehicle. Five prism layers were grown from the surface of the truck and six layers were
22 grown from the ground.

23 The filtered or averaged NSE can be solved within a specified computational domain at discrete
24 locations, determined by the locations of cells within the mesh. The size of the smallest
25 turbulent scales that can be resolved is limited by the size of the cell. Thus, it is necessary to
26 ensure that the cell size is sufficiently small enough to capture the smallest energy containing
27 eddies. This usually is ensured by the normalised wall distance, defined by $y^+ = n u_\tau / \nu$, where
28 $u_\tau = \sqrt{(\tau_w / \rho)}$ is the shear velocity, τ_w is the shear stress at the wall and n is the distance from
29 the first cell to the wall, in the normal direction of the wall surface face. 70% of the cells had a
30 y^+ value less than 3. However, there were a few cells at the front of the vehicle that had a
31 higher y^+ value which skewed the results producing large y^+ values. The mean values are
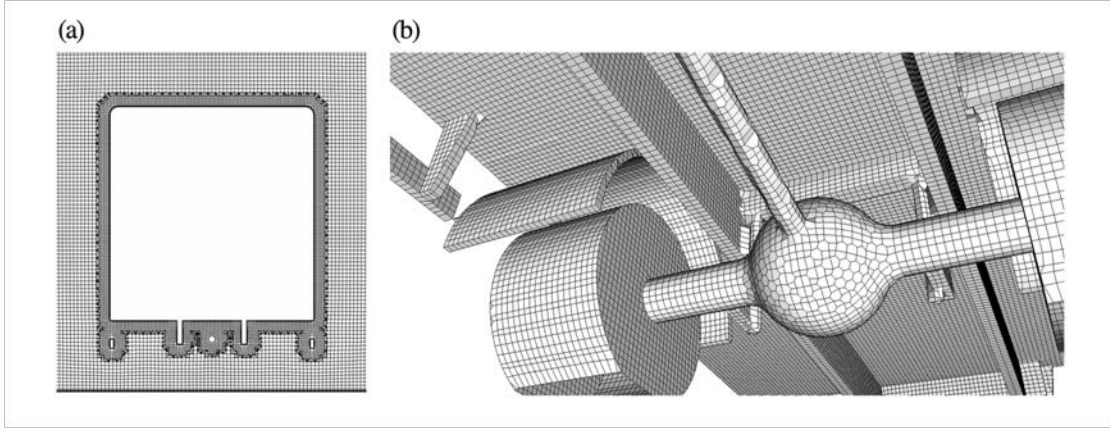32 given in table 1.

Fig. 3 (a) Cross section of fine mesh at *x*=0.5*l,* where *l* is the length of the vehicle. (b) Surface mesh underneath the truck.

Table 1 Average value for the normalised wall distance.

	LES Fine	LES Coarse	k-ω Fine	k-ω Coarse	k-ε Fine	k-ε Coarse
y^+	15.44	14.26	7.06	6.50	8.42	7.91

3.4. Numerical details

The governing equations of LES are discretised using Gaussian finite volume integration, which involves summing and interpolating values on cell faces. The time derivative is discretised using a backward method, which is a second-order implicit scheme. The convection, diffusion and subgrid components are discretised using second-order central difference schemes which ensure numerical accuracy. For the pressure-velocity coupling, the Pressure Implicit with Splitting of Operators (PISO) algorithm was employed. Additional details of this can be found in Issa (1986). For the RANS equations, the central difference scheme is used for the convection, diffusion, production, dissipation and destruction terms.

To ensure temporal stability at every iteration, the time step was adjusted such that the Courant number, $C_o = u\Delta t/\Delta x$ remained below 1. The convergence criteria for the pressure and velocity are set to $1\mathrm{x}10^{-6}$ and $1\mathrm{x}10^{-5}$, respectively. The velocity convergence criterion was usually satisfied on the first iteration whilst the pressure one took around 4 iterations. The mean time step in the simulation used was $t^* = 5.99\mathrm{x}10^{-3}$, where $t^* = tu_\infty/h$. The LES was started with a uniform internal field. The flow field is fully developed before time averaging can take place. Statistically stable solutions were obtained after $t^* = 384$ for the fine mesh and were averaged for a period of t^*=314, which is equivalent to 135 passes of a fluid particle over the length of the vehicle. The coarse mesh took $t^* = 1164$ and was averaged for $t^* = 1733$.

The convergence of all the RANS cases was based on the steady-state behaviour of the aerodynamic coefficients. Convergence was achieved after 3000 iterations for the coarse mesh case with realizable k-ϵ turbulence model, while 1000 additional iterations were required in the fine mesh case. When simulating using the SST k-ω turbulence model, the solution of the coarse mesh case reached convergence after 4000 iterations but the fine mesh case required in total 20,000 iterations to obtain a converged solution.

6

1   ### 3.5. Mesh sensitivity

2   To isolate the effects of mesh resolution in the simulations, mesh sensitivity tests were carried
3   out. Fig. 4 shows time-averaged velocity profiles in the slipstream of the vehicle in the LES for
4   both the fine and coarse meshes at $y = 0.58w$, taking w to be the width of the vehicle. The
5   velocity profiles are non-dimensionalised with respect to the free stream velocity. Both the fine
6   mesh and coarse mesh have shown a good level of agreement. Figure 5 shows the time-averaged
7   surface pressure coefficient along the centre of the truck, for both the fine and coarse meshes.
8   The coefficient of pressure has been defined by:

9    $$C_p = \frac{<\bar{p}> - p_\infty}{\frac{1}{2}\rho_\infty u_\infty^2}, \qquad (9)$$

10   here $<\bar{p}>$ is the time-averaged pressure distribution, p_∞ is the freestream pressure, ρ_∞ is the
11   freestream fluid density, and u_∞ is the free stream velocity. The free stream pressure reference
12   was taken from a cell in the top corner at the inlet. A good level of agreement is found between
13   the fine and coarse meshes in both the front cab and trailer box. Additional surface pressure
14   comparisons between the fine and coarse meshes have been carried out in the following section.
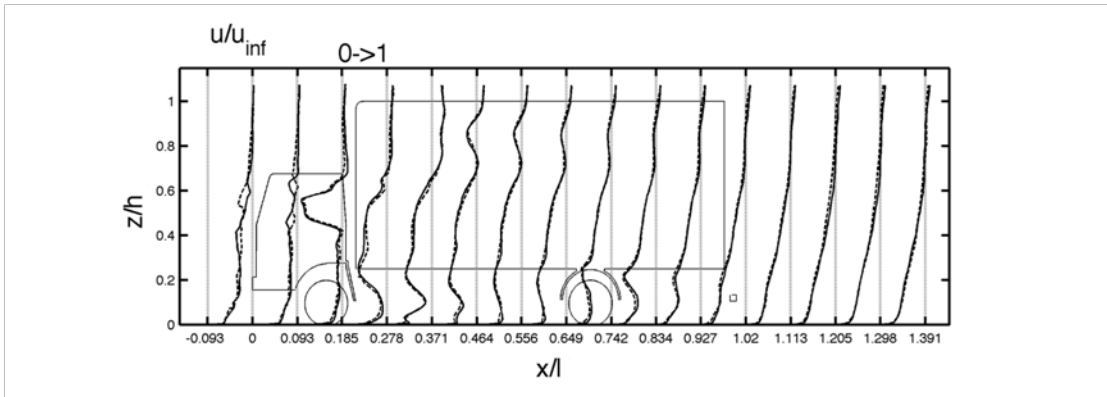
15
16   Fig. 4 Time-averaged velocity profiles in the slipstream of the vehicle at a distance of $0.08w$ from the
17   side of the box where w is the width of the trailer box, for the fine mesh (solid curve) and coarse mesh
18   (dashed curve).
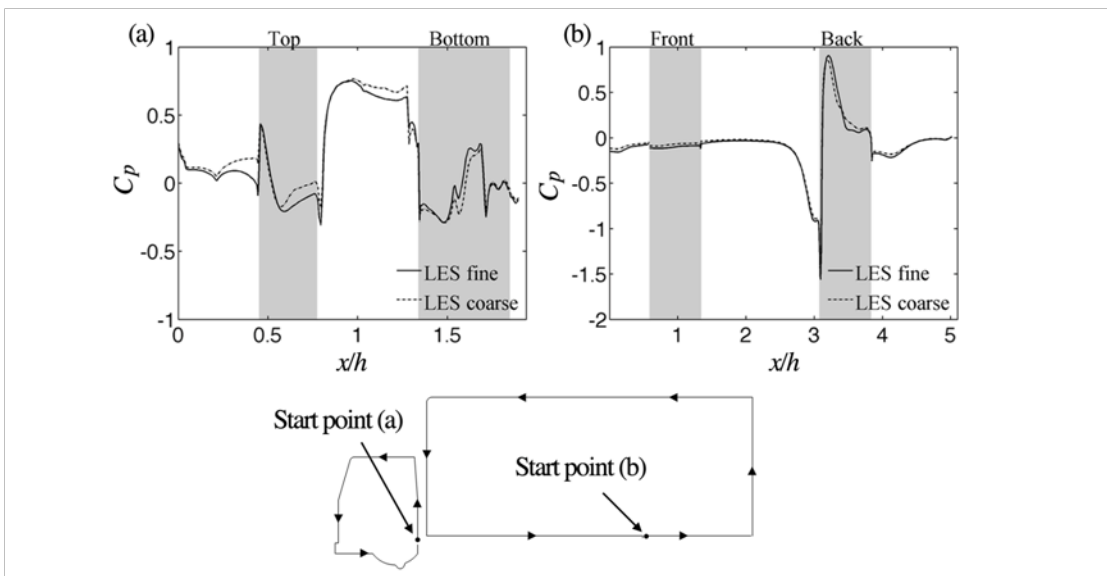
19
20   Fig. 5 Comparison of the time-averaged surface pressure coefficients along a cross section through the
21   centre of the truck. x is the distance around the cab or trailer, and it has been scaled by the height of the
22   vehicle, h (a) Front cab. (b) Container box.

23   ## 4. Validation

7

Quinn et al. (2007) carried out full-scale experiments on the truck, in which the real-time wind velocity and direction were collected using an ultrasonic anemometer. The full-scale data used in the current work is from the static measurements, where the anemometer was mounted on a separate upstream mast. There is no impact on the surface pressures as the location is not upstream of the surface pressure locations. The interference will be small because the size of the anemometer is small compared to atmospheric turbulence. Throughout the study, 45 static pressure tapping points were mounted flush against the surface of the truck. What follows is a reanalysis of the raw data collected in the study. The surface pressure data collected in the experiments were used to validate the simulation results. The locations of the tapping points used in the experimental work are shown in Fig. 6. Taps 1 to 9 are located $0.609h$ from the front of the trailer box, where l is the length of the trailer box. Following taps were placed at $0.724h$, $1.199h$, $1.674h$ and at $2.149h$. On the side faces, the rows of tapping points are $0.114h$ away from the top and bottom edges, with the centre tap positioned midway between the two rows. On the roof, the rows of tapping points are $0.114h$ from the side edges, with the centre tapping point along the middle of the vehicle.

During the experimental tests, only 12 pressure probes were collecting data at any given time, as such a large number of runs were carried out with probes connected in various combinations of locations. The pressure data was calibrated to account for the drift effect. There were periods of time where the data was not reliable, due to significant wind direction fluctuations or inadequate dynamic pressure readings during averaged intervals of 1 minute. To account for that, the data was filtered to ensure that only the surface pressure for which the wind was blowing in a suitable direction and speed would be considered. If the averaged data fell within a window of +/-7.5 degrees from a headwind and the dynamic pressure, $q = \frac{1}{2}\rho U^2$ was above $15 \mathrm{kgm^{-1}s^{-2}}$, then the data was deemed suitable. From the remaining data, mean pressure coefficients associated with each tapping point was calculated and standard deviations of the mean coefficients were calculated. Figures 7a-7e show the results with error bars indicating +/-1 standard deviation. Theta has been taken to be an angle from the bottom of the container to the positions around the truck in an anticlockwise direction facing the front of the truck. It should be noted that experimental data does not exist for all taps, as previously mentioned only 12 pressure probes were collecting data at any given time. Thus, when filtering results there were only a small number of runs that were suitable for analysis.

For each of the simulation results, five cross sections were taken along the trailer box and the coefficient of pressure was calculated using equation (9). The pressure coefficients in the fine mesh simulation were averaged for 167 seconds, which is equivalent to 22.4 times the so-called large-eddy turnover time (h/u_∞). The difference in simulation times when compared to the full-scale experiments is believed to be small.
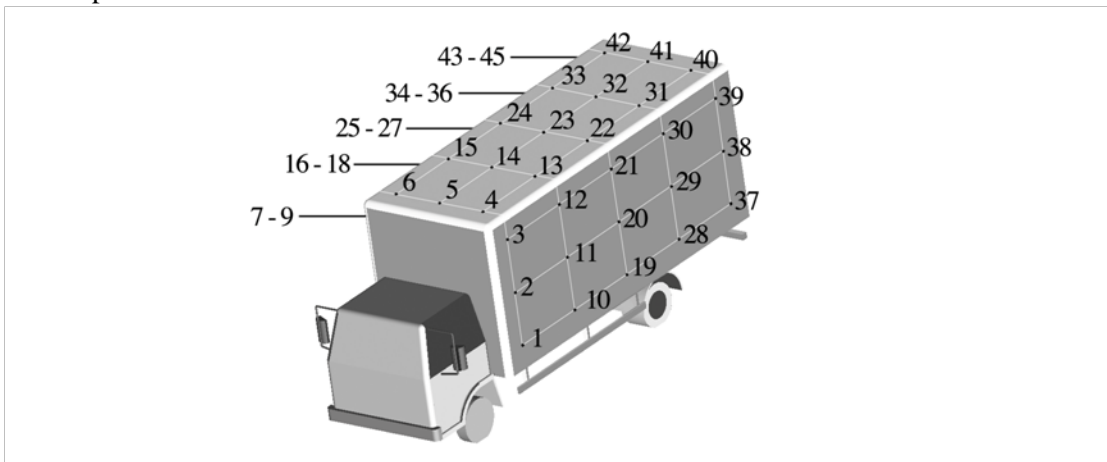

Fig. 6 Location of pressure taps.

1   The comparisons made in Fig. 7 show a reasonable level of agreement between the full-scale
2   experiments and the LES simulations for both the coarse and fine mesh. However, it can be
3   seen, in the first two cross sections that the RANS simulations underestimated the low pressures
4   seen at the front of the truck. This is due to RANS models struggling to predict airflows close
5   to separation regions where high level of turbulent activities exist. The Experimental data
6   reflects the separation bubbles found at the leading edge. In this region, pressure fluctuates
7   rapidly and is indicated by the large standard deviations found on the roof and on the top half
8   of the sides of the vehicle, whilst for the lower pressure taps, i.e. taps 1 and 9, lower standard
9   deviations indicate that the air is less turbulent.

10   Fig. 7b implies that the weakest level of agreement between CFD and experimental results
11   occurs at the second cross-section. The natural wind is not steady and is potentially gusty. This
12   may play a pivotal role in the flow behaviour in this region. The fact that the uniform wind
13   condition in the simulation is different than the realistic wind may have contributed greatly to
14   the discrepancies in the comparison. It is worth noting that this region is known to be highly
15   turbulent and is strongly Reynolds number sensitive (Hoxey et al., 2002, Richards and Quinn,
16   2002). Thus, the local Re difference between the full-scale experiment and small-scale
17   simulation may lead to the discrepancies in the results locally in this region.

18   In Figs. 7c-7e, a good level of agreement is obtained with relatively smaller standard deviations.
19   For all the cross-sectional loops, the overall standard deviation of each loop decreases from the
20   front of the truck to the back, which is due to the development of slipstream. To be more specific,
21   as the flow travels further downstream after separation at the front edge, the reattachment
22   occurs which reduces the level of turbulent intensity. Therefore, the fluctuation of the surface
23   pressure close to the rear of the truck would be less significant.
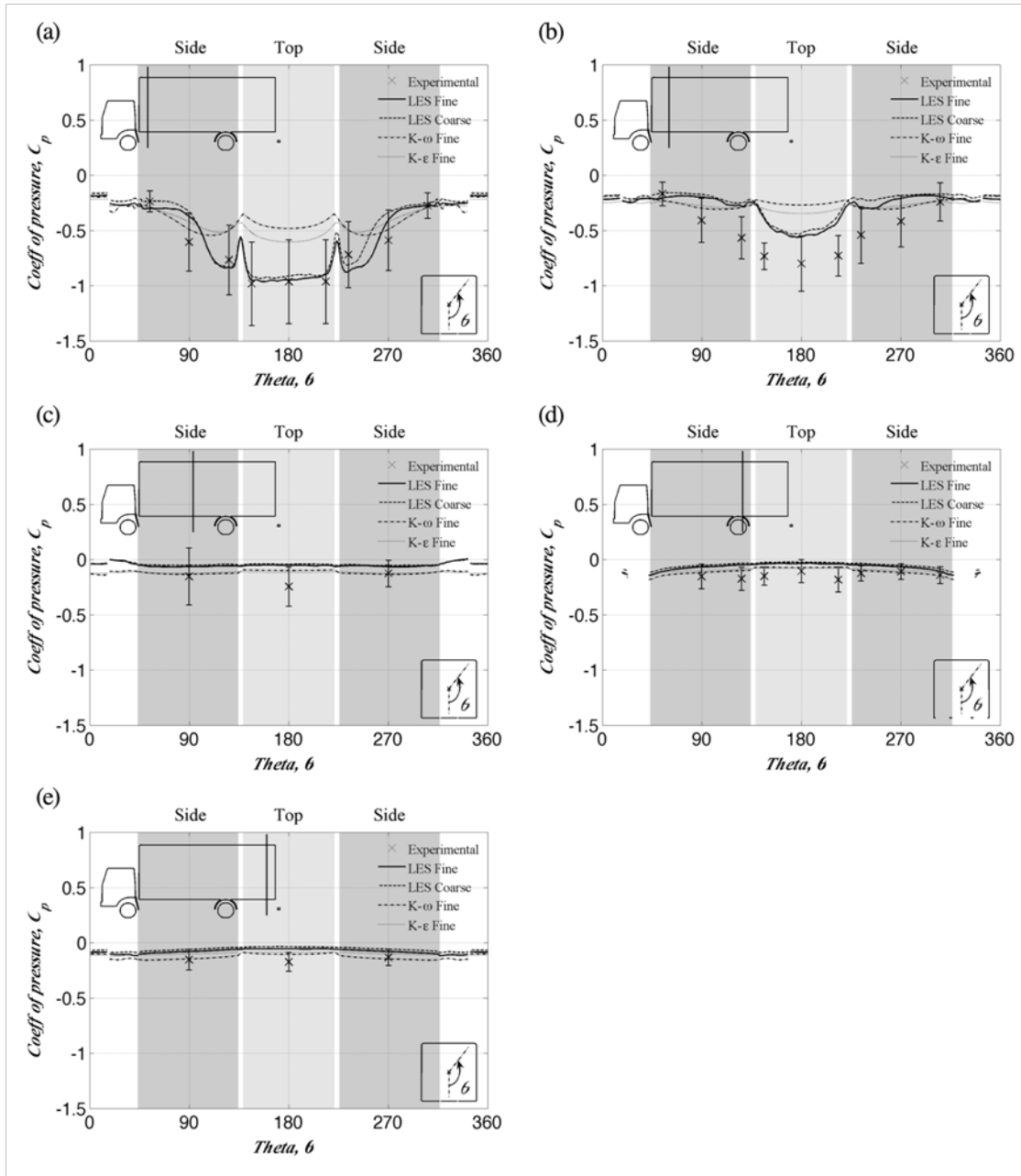
Fig. 7 Cross-sections taken along the container box (a) x=0.609*h*, (b) x=0.724*h*, (c) x=1.199*h*, (d) x= 1.674*h*, (e) x=2.149*h*.

5. Aerodynamic forces and moments

By integrating the surface pressure, the aerodynamic forces and moments from the simulations can be obtained. Figure 8 shows the definition of the coordinate system as well as the sign convention, where F_d, F_l and F_s are the drag, lift and side forces, respectively and M_r, M_y and M_p are the rolling, yawing and pitching moments, respectively. The moments have been taken about the middle of the truck at ground level at $x=0.5l$.
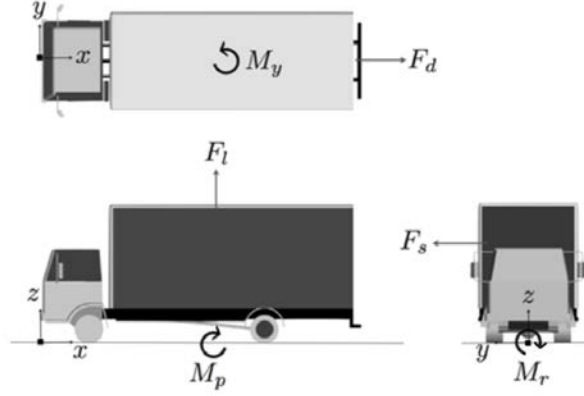
1

2   Fig. 8 Forces and moments sign convention used.

3 The drag coefficient, C_d, the lift coefficient, C_l, and the side force coefficient, C_s, are defined
4 as:

5   $C_d = \dfrac{F_d}{\frac{1}{2}\rho u_\infty^2 A}\,,$ $C_l = \dfrac{F_l}{\frac{1}{2}\rho u_\infty^2 A}\,,$ $C_s = \dfrac{F_s}{\frac{1}{2}\rho u_\infty^2 A}\,,$ (10)

6 where A is the reference surface area, which has been taken to be the cross-sectional area of the
7 vehicle normal to the x axis. The rolling moment coefficient, C_r, the yawing moment coefficient,
8 C_y, and the pitching moment coefficient, C_p, are defined as:

9   $C_r = \dfrac{M_r}{\frac{1}{2}\rho u_\infty^2 A h}\,,$ $C_y = \dfrac{M_y}{\frac{1}{2}\rho u_\infty^2 A h}$ and $C_p = \dfrac{M_p}{\frac{1}{2}\rho u_\infty^2 A h}\,.$ (11)

10 Table 2 shows the aerodynamic coefficients obtained for each of the simulations. For a truck
11 subjected to headwinds, it is expected a statistical average of the side forces, rolling, and yawing
12 moments to be zero, as indeed it is based on the LES and RANS results. Regarding the
13 aerodynamic forces, no oscillations were found in the RANS simulations using the $k-\epsilon$ model,
14 while only minor oscillations were observed from the simulations with the $k-\omega$ model.
15 Noticeable oscillatory behaviour was found for the aerodynamic forces obtained from the LES
16 simulations, which will be investigated in more detail later.

17 Table 2 Comparison of the aerodynamic coefficients.

	LES Fine	LES Coarse	k-ω Fine	k-ω Coarse	k-ε Fine	k-ε Coarse
Cd Ave	0.56	0.52	0.86	0.87	0.62	0.63
Cd Std	0.02	0.02	0.00	0.00	0.00	0.00
Cl Ave	0.10	0.10	-0.07	-0.11	0.07	0.07
Cl Std	0.02	0.03	0.00	0.00	0.00	0.00
Cs Ave	0.00	0.00	0.00	0.00	0.00	0.00
Cs Std	0.02	0.03	0.02	0.02	0.00	0.00
Cr Ave	0.00	0.00	0.00	0.00	0.00	0.00
Cr Std	0.01	0.02	0.01	0.01	0.00	0.00
Cy Ave	0.00	0.00	0.00	0.00	0.00	0.00
Cy Std	0.02	0.02	0.00	0.00	0.00	0.00
Cp Ave	0.39	0.35	0.46	0.47	0.36	0.37
Cp Std	0.02	0.03	0.00	0.00	0.00	0.00

6.   Flow structures around the truck
6.1. Surface trace lines

3   By plotting the time-averaged streamlines, it is possible to identify the critical points within a
4   flow. These are points of equilibrium where the spatial first and second derivatives are zero.
5   More details of critical point analysis can be found in Perry and Chong (1987). Figs. 9a and 9b
6   show the time-averaged streamlines on the surface of the truck for the fine mesh and coarse
7   mesh, respectively. *Sp*1 represents the stagnation point generated at the front of the vehicle,
8   which is located in the centre at 0.46*h* above the ground for the fine mesh and at 0.48*h* for the
9   coarse mesh. As the flow separates and reattaches to the surface of the truck, these points
10 collectively generate bifurcation lines and are shown along the top and sides of the vehicle.
11 Bifurcation lines can either be positive or negative depending on the direction in which
12 streamlines are pointing. Each pair of bifurcation lines are known to generate a recirculation
13 region, which is shown by *PBL*1 (runs along the top and down the sides of the container at the
14 leading edge) and *NBL*2 for the side separation bubble. *PBL*1 and *NBL*3 generate the roof
15 separation bubble. *Xb*1 is the maximum distance between where the flow separates and
16 reattaches near the front edge of the truck box. The length is 0.33*h* for the fine mesh and 0.35*h*
17 for the coarse mesh. The surface flow details show to some extent similarity with a benchmark
18 study (Krajnović and Davidson, 2003) on the flow around a bluff-body shape with square back.
19 This simplified shape was originally used by Duell and George (1999) who believed that it can
20 "generate the near wake structure of a typical ground vehicle". In the current work, *Xb*1 found
21 in the fine mesh case is surprisingly identical to that found in Krajnović and Davidson (2003),
22 despite the obvious difference in the nose region of the two models. In addition, the position of
23 the stagnation point is analogous to that observed by Krajnović and Davidson (2003). The
24 current finding seems to suggest that this strongly simplified bus-like shape in the literature
25 could predict similar stagnation point at the nose and separation bubble at the front edge of a
26 realistic vehicle shape with a bluff body studied in the present work. In these simulations, the
27 side separation bubble is much smaller, which is believed to be due to the cab at the front
28 disturbing the flow field before it reaches the container. As a result, *Xb*2 is smaller and has a
29 length of 0.21*h* for the fine mesh and 0.25*h* for the coarse mesh.
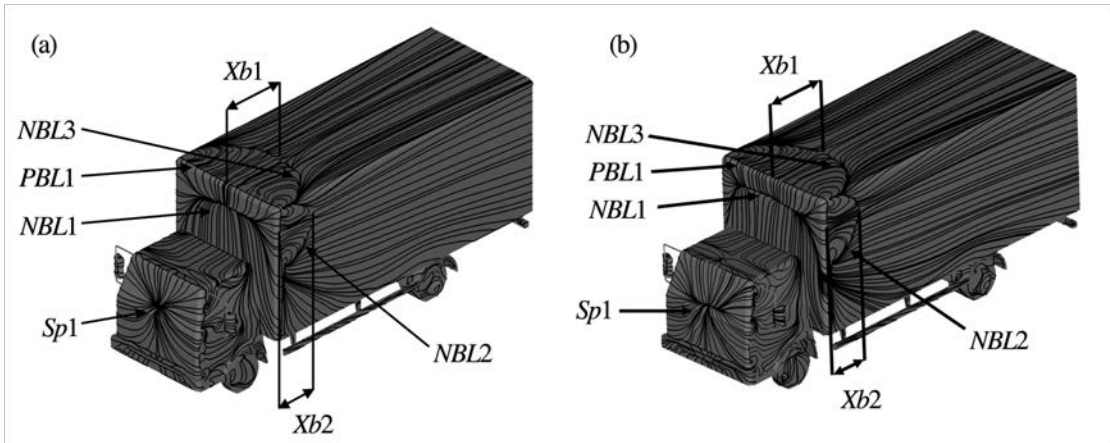

30

31   Fig. 9 Time-averaged trace lines on the surface of the vehicle, indicating the stagnation point at the
32 front of the vehicle, the positive and negative bifurcation lines associated with the separation bubble on
33   the roof and the side of the container. (a) Fine mesh. (b) Coarse mesh.

34 Figs.10a and 10b show the isosurface of the coefficient of pressure, $C_p = -0.14$ generated in the
35 wake of the vehicle for the fine and coarse mesh, respectively. The coarse mesh simulations
36 failed to pick up the arch-shaped vortex structure in the wake of the truck. Given that LES
37 resolves the flow at each grid point and models the subgrid components, it is unsurprising that
38 a mesh with more cells contains more detailed flow features. Moreover, this implies that an
39 isosurface of the pressure coefficient may not be sufficient to identify vortex structures and that
40 the pressure coefficient is a highly sensitive parameter. Nonetheless, the isosurface around the

truck from the fine mesh is similar to that around a simplified cuboid shape found by Krajnović and Davidson (2003). It is worth mentioning that the vortex shape in the wake is a 'U' shape in the present work while a closed ring shape was identified by Krajnović and Davidson (2003). This is due to the flat underbody geometry for the strongly simplified model. It is believed that the turbulence created under the truck in the present work by the underbody features, such as engine, chassis, gearbox and transmission shaft, would disrupt the flow either breaking the vortex ring as shown in Figure 10 of Krajnović and Davidson (2003) or substantially deform its existence as shown in Fig. 10a below.
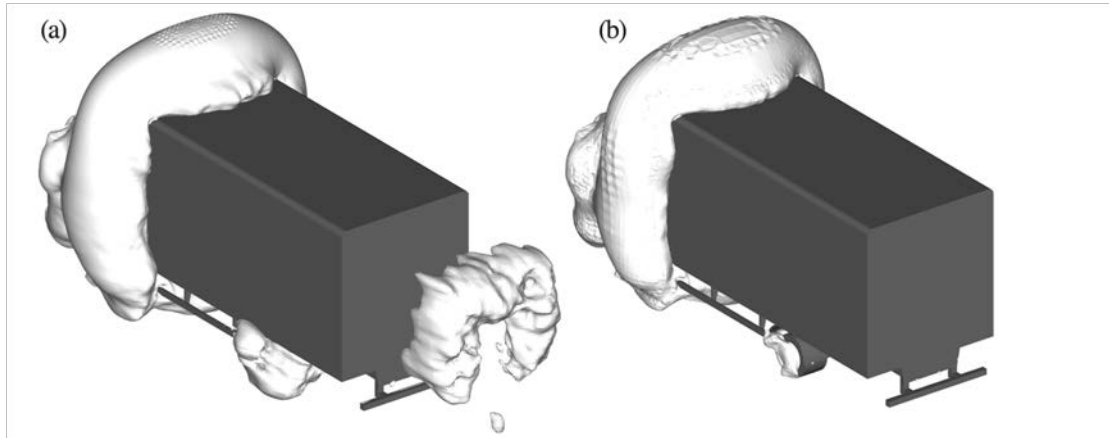

Fig. 10 (a) and (b) Isosurface for the time-averaged coefficient of pressure, C_p= -0.14, for the fine and coarse meshes respectively.
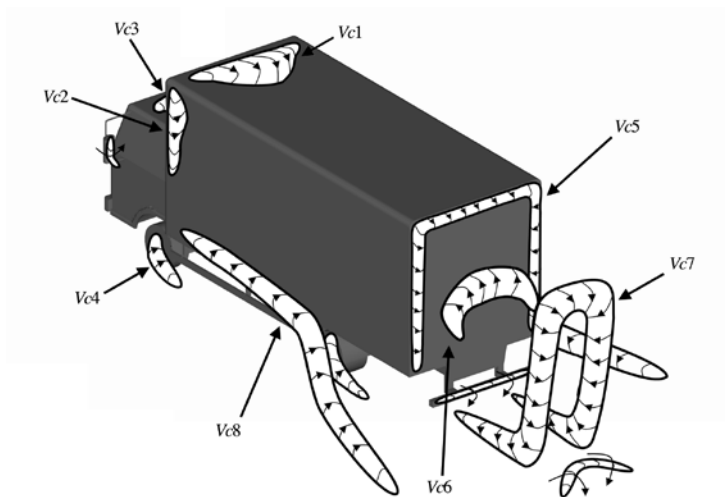
6.2. Time-averaged flow structures

To visualise the time-averaged vortex cores, a tool developed by Sujudi and Haimes (1995) has been adopted. The method is based on critical point theory, which identifies the centre of swirling flow by evaluating the eigenvalues of the velocity gradient tensor. Fig. 11 shows the implementation of this technique.
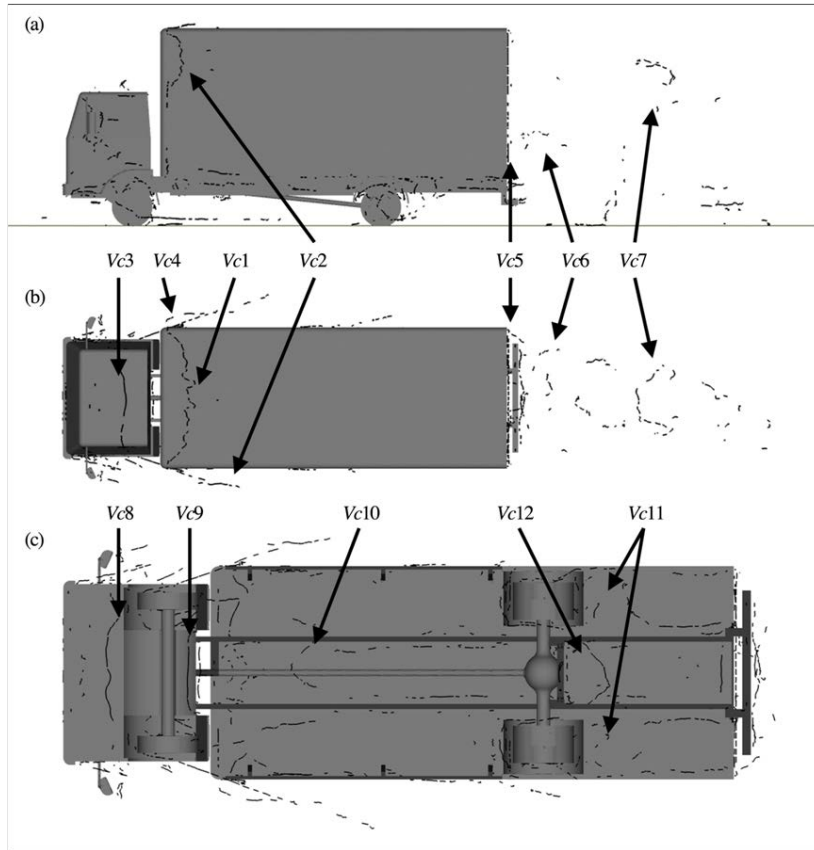
Fig. 11 Vortex cores of the time-averaged flow from the fine mesh (a) Side view (b) Top view (c) underbody view.

Fig. 12 Schematic representation of the dominant time-averaged vortex structures.

Fig. 12 shows a schematic representation of the dominant vortex cores. *Vc*1 is a vortex that is generated at the leading edge of the truck, which is later reattached to the top surface. *Vc*2 shows the location where vortices are shed off both sides of the truck. The dominant instantaneous structures generated in both *Vc*1 and *Vc*2 are known as hairpin vortices, which have been well documented in (Krajnović and Davidson, 2003). *Vc*3 shows a circulation region generated by a strong positive pressure at the front of the container box. *Vc*4 has been generated by the airflow past the wheels of the truck. The flow structure originates from underneath the truck and pushes air through between the mud shield and wheels. *Vc*5 is generated around the

14

trailing edge of the truck container box and represents the initial recirculation region in the wake of the flow. Due to the low pressures found behind the truck, air sinks down from the top, and air from underneath the truck between the wheels pushes up creating $Vc6$, which is a large backward circulation region that rotates in the opposite direction to $Vc5$. $Vc7$ is generated by the accumulation of vortices in the wake of the truck.

The circulation regions around the vortex cores can be observed by plotting the streamlines and velocity vectors on cross-sectional planes at various locations around the vehicle. Figs. 13 and 14 show the cross sections parallel to the side of the vehicle, with Fig. 14 detailing the underbody flow structures. Fig. 13a and 14a cut the truck through the centre, while Fig. 13h and 14h show the flow characteristics along the side slipstream of the vehicle. Figs. 15 and 16 show the cross-sections parallel to the ground, with Fig. 16 detailing the underbody flow structures.

Figs. 13a-13e shows $Vc6$ spanning the width of the vehicle before the air from the side slipstream breaks the structure apart at $y=0.90w$. Figure 15 suggests that the dominant vortex in the wake of the vehicle is represented by $Vc7$. $Vc7$ originates from a position close to the ground at $z=0.054h$, as is shown in Fig. 15a. It grows upward along the rear of the truck to form a recirculation region, as can be seen in Figs. 15a-15g. As it approaches further upward at around $z=0.805h$, the air from the roof of the vehicle forces the top of the vortex to rotate away from the vehicle which can also be observed in Fig. 13a, generating the arched shape structure indicated in Fig. 10. It is worth noting that in Fig. 15f, there is a small level of asymmetry in $Vc7$. More symmetric flow could be obtained by running simulations for a longer period of time. However, this would come at a large computational cost for a relatively small improvement in the quality of results.

Figures 14 and 16 highlights the complexity of the underbody flow structures. In Figure 14a, $Vc8$ is a vortex generated due to flow separation that occurs at the bottom edge of the front of the driver cab. The curvature of the engine shape generates $Vc9$. $Vc10$ is generated by the cab and transmission shaft. $Vc11$ is generated by the rear wheels, which originates at around $z=0.114h$ and extends until the top of the chassis, as shown in Fig 16c. $Vc12$ is created because of the cross bracing beam that joins the two longest beams of the chassis together, forcing the air into the confined space. $Vc13$ in Fig. 16d is located in line with the chassis at $z=0.172h$ and is the result of the disturbance of the air behind the front mudguards. $Vc14$ shown in Fig. 16c has originated from the gap in the centre of the wheels close to the wheel hub. $Vc15$ in Fig. 14f has been generated because the air is forced out between the cab and the storage container into the slipstream.
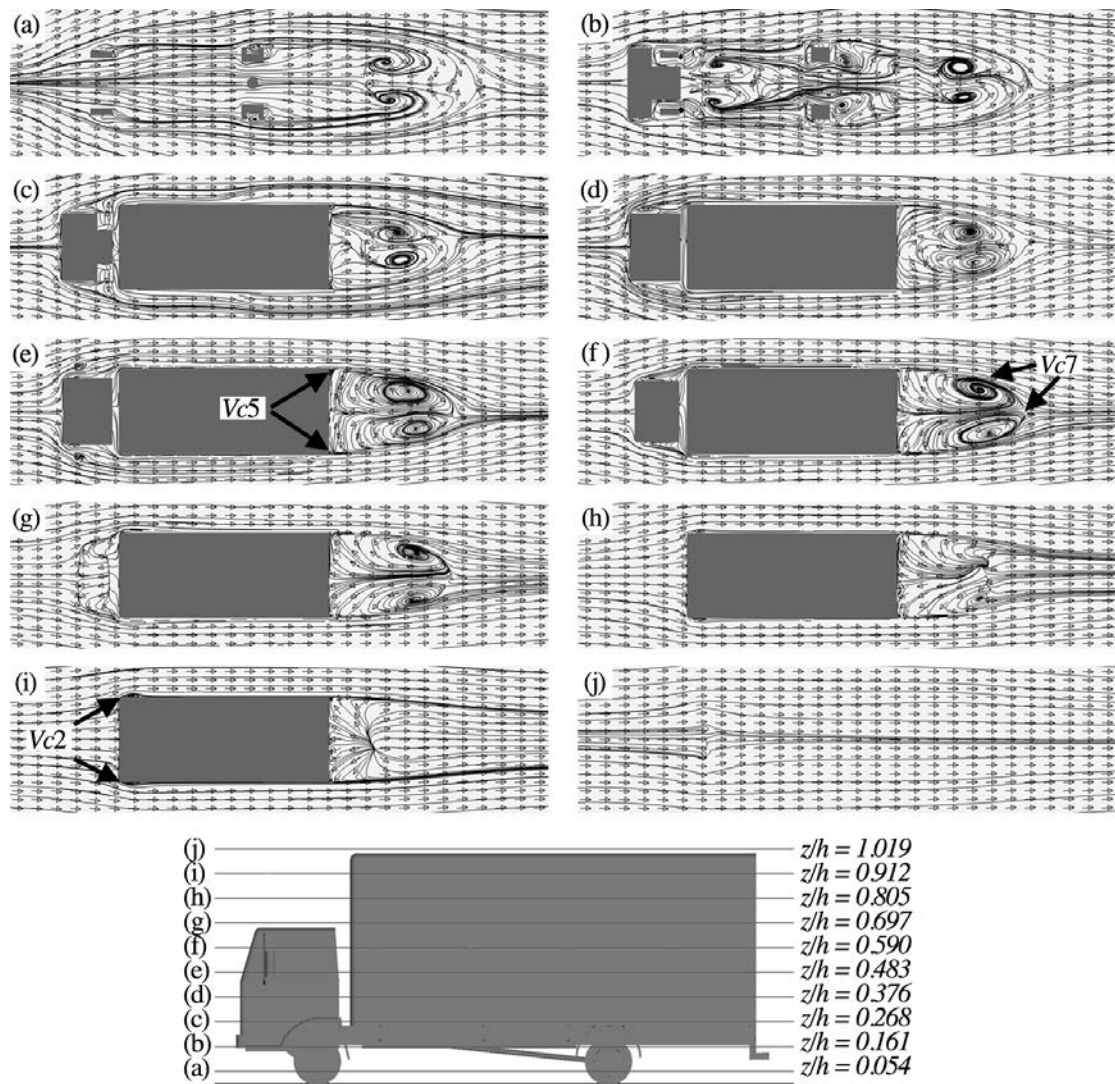
1
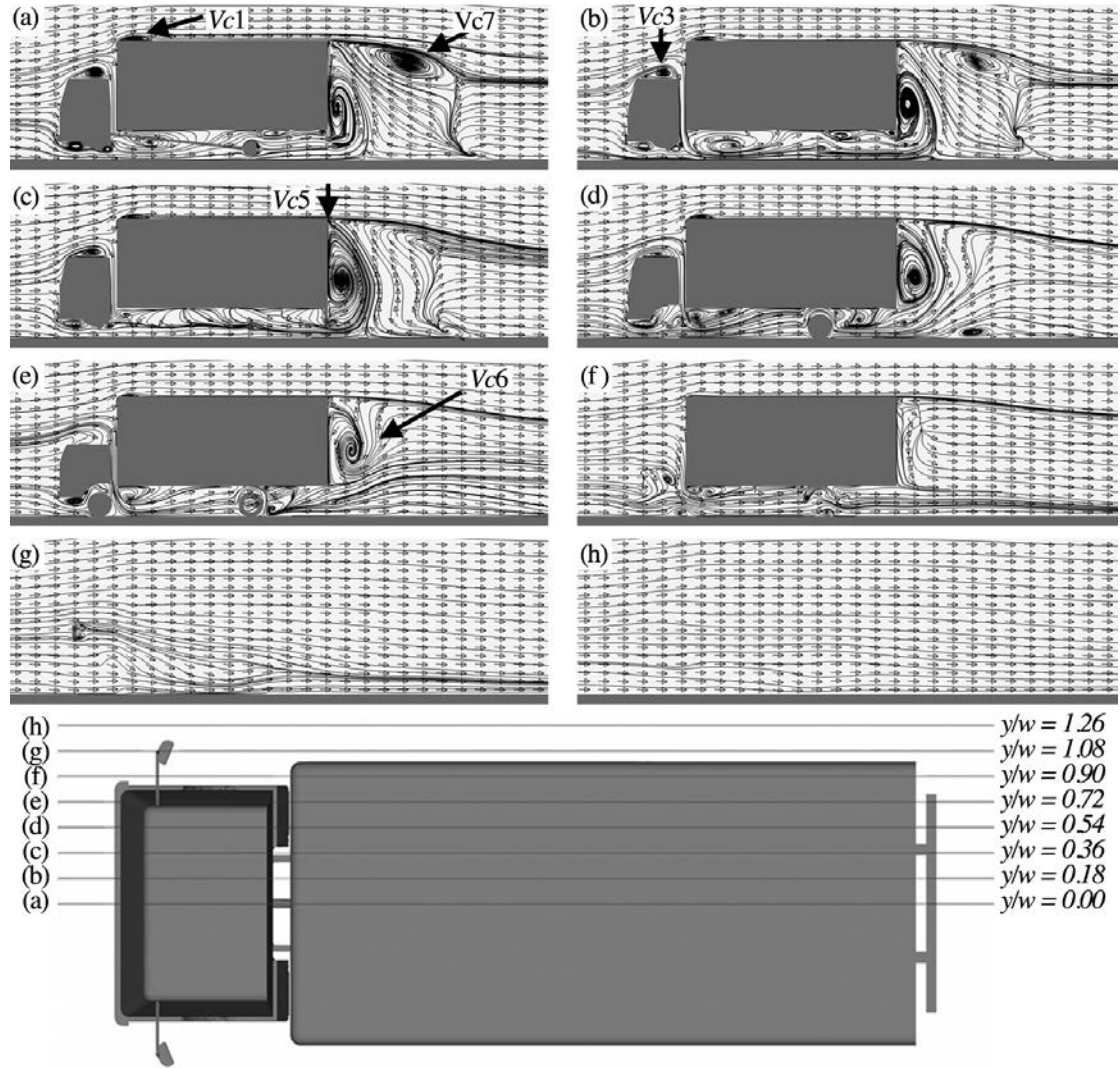
2 Fig. 13 Time-averaged velocity vectors and streamlines on cross-sectional planes parallel to the sides
3 of the truck from the fine mesh, where *w* is half the width of the truck box.

4
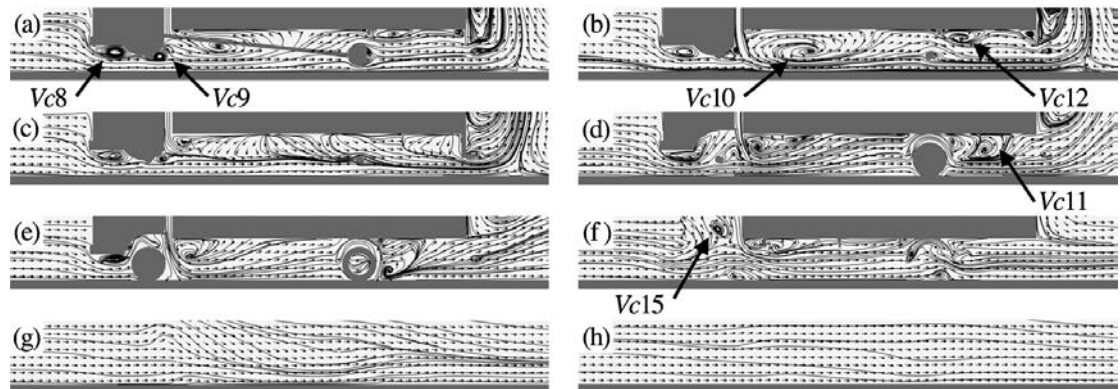
5 Fig. 14 Time-averaged velocity vectors and streamlines on cross-sectional planes parallel to the sides
6 of the truck for the fine mesh. Figures 14a – 14h represent the same locations of the cross-sections as
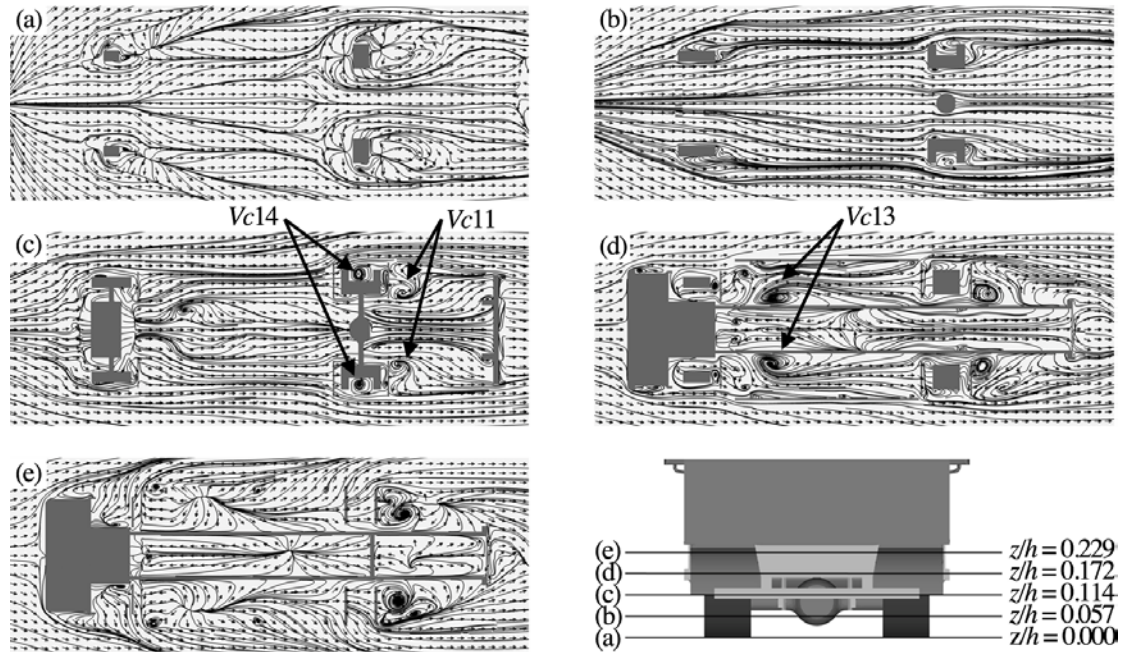7 shown in Fig. 13.

1

Fig. 15 Time-averaged velocity vectors and streamlines on cross-sectional planes parallel to the side of
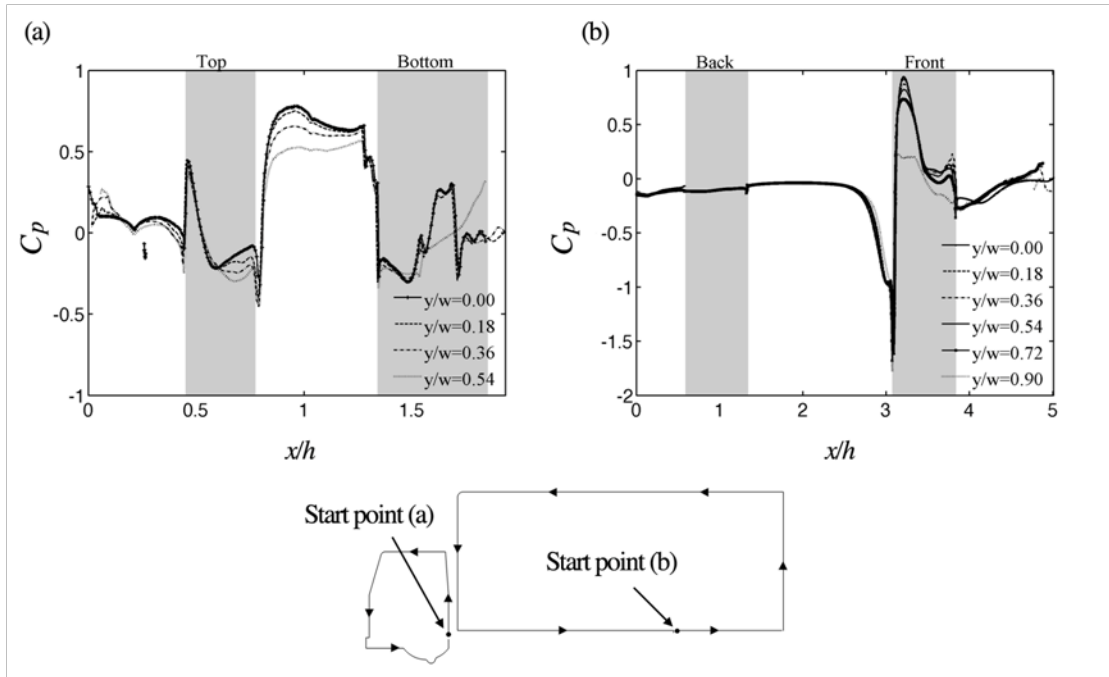the truck from the fine mesh.

Fig. 16 Time-averaged velocity vectors and streamlines on cross-sectional planes parallel to the
ground, here results have been taken from the fine mesh.

6.3. Time-averaged pressure

The surface pressure of the truck was probed and the pressure coefficient was calculated using
equation (9). Fig. 17a shows the pressure coefficient at a number of locations around the truck
cab, starting at the back of the cab near the bottom travelling in an anticlockwise direction. At
the top surface in the range $0.06 < d < 0.11$, there are two peaks with different sizes. The larger
peak is generated close towards the back at the top of the vehicle, while the smaller one has
been generated due to the separation region found at the leading edge of any bluff body and has
been created by the vortex core $Vc1$ in Fig. 12. Significant high pressures are found on the front
of the vehicle as expected. It should also be noticed that there is a deviation for $y=0.54w$
underneath the truck which is due to the geometry changes. This change can be seen in Fig.
13d. Fig. 17b shows the pressure coefficient around the container box, starting midway
underneath the truck travelling in an anti-clockwise direction at different cross-sections along
the truck. It appears that a similar pressure profile exists throughout the width of the vehicle.

18

Fig. 17 Time-averaged surface pressure distributions from the fine mesh. x is the distance around the cab or the container. (a) Front cab (b) Container box.

Fig. 18 shows the distribution of the time-averaged pressure coefficient on the underbody surface, where high pressure is signified by dark regions and low pressure is represented by lightly coloured regions. Fig. 18, together with the details of the underbody structures given in Fig. 14 and 16, provides useful information for a variety of applications from investigating regions where vehicle drag can be improved to driving load space ventilation for the transportation of livestock (Hoxey et al., 1996).
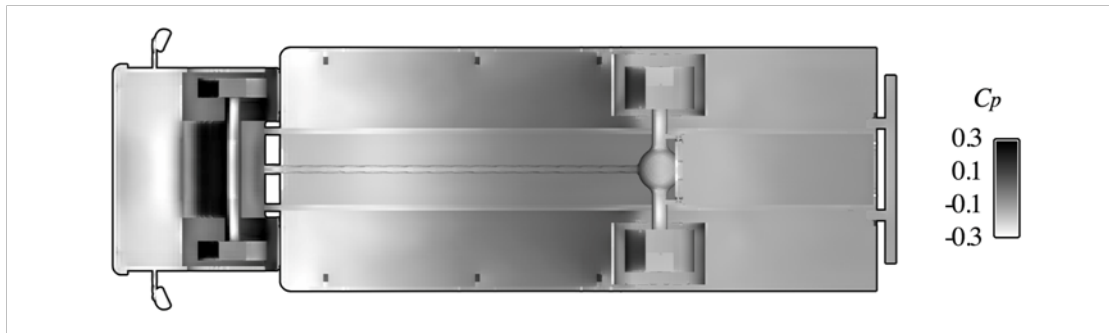
Fig. 18 Time-averaged underbody surface pressure distribution from the fine mesh.

6.4. The temporal development of vortex structures

Figure 19a shows the instantaneous flow field visualised by plotting the isosurface of the pressure coefficient. However, this also includes regions where centrifugal forces are in equilibrium with viscous forces and thus does not explicitly show where vortex cores are. Hunt (1988) proposed a method for identifying vortex structures that are based on the foundations that a structure must have net vorticity and net circulation and that coherent structures must be Galilean invariant. The method proposed was defined by the second invariant of the velocity gradient tensor, also known as the Q –criteria:

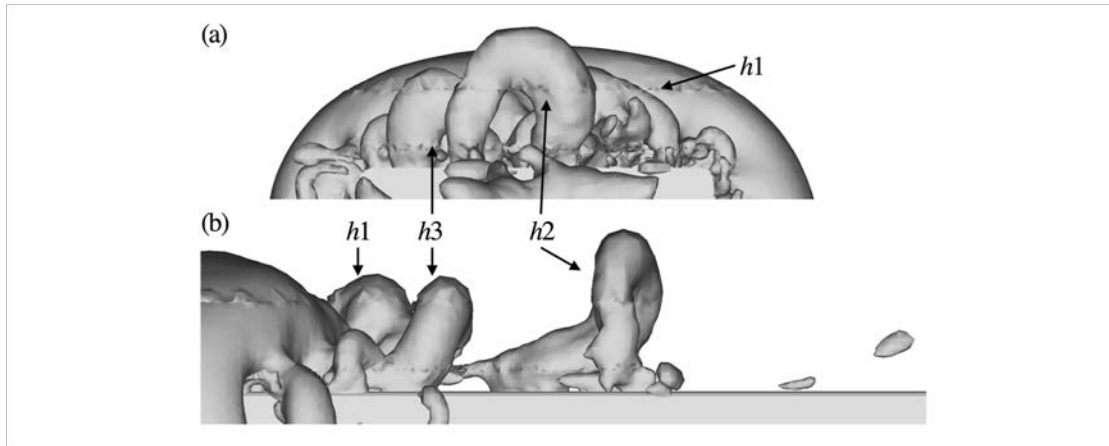$$Q = -\frac{1}{2}u_{i,j}u_{j,i}.$$

(12)

1   Figs. 19b, 19d and 19f show the temporal development of the isosurface for the coefficient of
2   pressure equal to -0.1. Figs. 19c, 19e and 19g illustrate the temporal development of the vortex
3   structures for Q=1200. The dimensionless time between each frame is t^*=1.03.
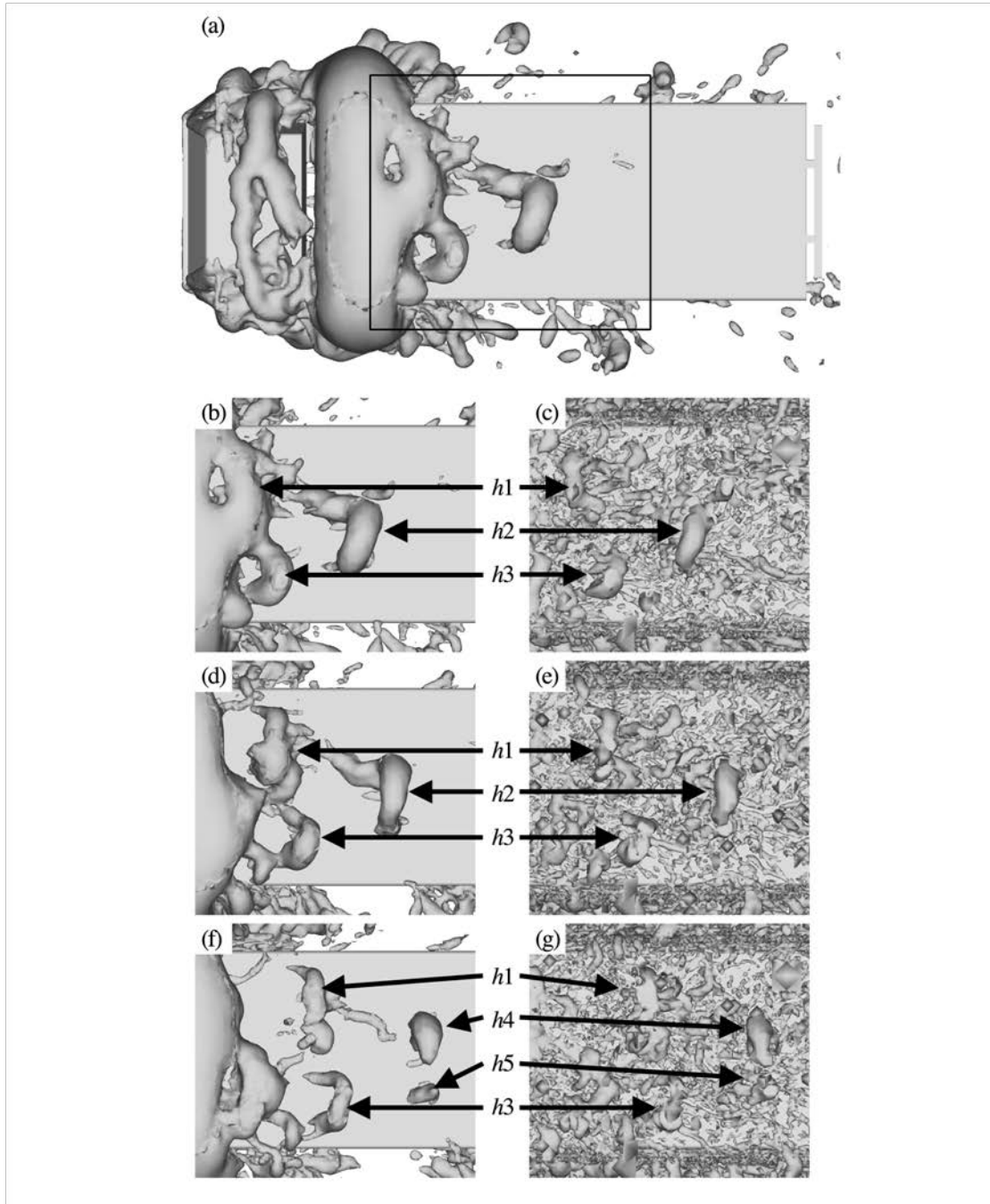
4

5   Fig. 19 Instantaneous flow features from the fine mesh (a) Isosurface for C_p=-0.1. (b)-(g) Show a close
6   up of (a). (b), (d) and (f) show an Isosurface for C_p=-0.1. (c), (e) and (g) Show the Isosurface for the
7   second invariant of the velocity gradient tensor, taking Q=1200.

8   Hairpin vortices are observed, as indicated by $h1$, $h2$ and $h3$ in Fig. 19, which are generated at
9   the leading edge of the container box. As time increases, the vortex structures propagate
10 downstream along the top of the container. The centre of the structure is elevated whilst the
11 legs remain connected to the surface of the truck. This can be seen more clearly in Fig. 20.
12 Eventually, the energy in the vortex structure dissipates and the top centre of the structure is

20

1   broken leaving two legs still attached to the truck. Consequently, *h2* breaks down into *h4* and
2   *h5*, as shown in Figs. 19f and 19g.

7.   Spectral analysis

7   As coherent structures continually attach and detach from the surface of the vehicle, the
8   aerodynamic forces and moments fluctuate in time. The time histories of the aerodynamic
9   coefficients have been used to calculate the vortex shedding frequencies around the truck
10 through spectral analysis. The Power Spectral Densities (PSD) is calculated by applying a
11 hanging window over the time-varying signal. A Fourier Transform (FT) of the signal is taken
12 and multiplied by the conjugate of the FT. The time histories of the aerodynamic coefficients
13 are shown in Figs. 21 and 22, for the fine and coarse meshes, respectively. The power spectrum
14 has been plotted against the Strouhal number, $St = fh/u_\infty$ where f is the frequency of the
15 periodic flow field motions of vortex shedding. A dominating frequency is found for the drag,
16 lift and side force coefficients in both the fine and coarse mesh cases at St≈0.05, which
17 represents the mean fluctuating frequency of the vortex in the wake of the vehicle.

18 Fig. 21b suggests that four dominant frequencies exist for drag. However, the physical
19 existence of the first low-frequency peak is unreliable, as the simulation has not run for a
20 sufficiently long enough period of time to be able to pick up such a low frequency. It should be
21 noted that a Strouhal number of 0.02 corresponds to around 3 cycles while a Strouhal number
22 of 0.05 corresponds to around 7 cycles. The second two peaks at St≈0.05 and St≈0.09 are the
23 dominant low-frequency shedding cycles. They are comparable to the large scale vortex
24 shedding seen in the wake of the vehicle. Data was collected for a longer period of time for the
25 coarse mesh simulations. As a result, very low-frequency oscillations are picked up, which is
26 also reflected in the time history for the aerodynamic coefficients. The dominant peak at
27 St≈0.09 in the fine mesh exhibits less energy than that in the coarse mesh. The reason for that
28 could be that by resolving the smaller scales in the fine mesh, the influence of the largest scales
29 on the smaller scales are maintained and when interacting with the surface of the vehicle they
30 contain significant amounts of energy. In both the fine and coarse meshes high-frequency
31 modes occur at St≈0.2. This represents the smaller structures interacting with the surface of the
32 vehicle and shows that they too contain significant amounts of energy.

33 As to the coefficient of lift, Cl, there are a large number of peaks in the range 0.05<St<0.5 for
34 both the fine and coarse meshes. This can be attributed to a wide range of vortices interacting
35 on a range of different scales with the underbody geometry. In terms of the side force coefficient,
36 one dominant low-frequency peak is identified at St≈0.05 while a range of high frequencies is
37 found in 0.15<St<0.4.
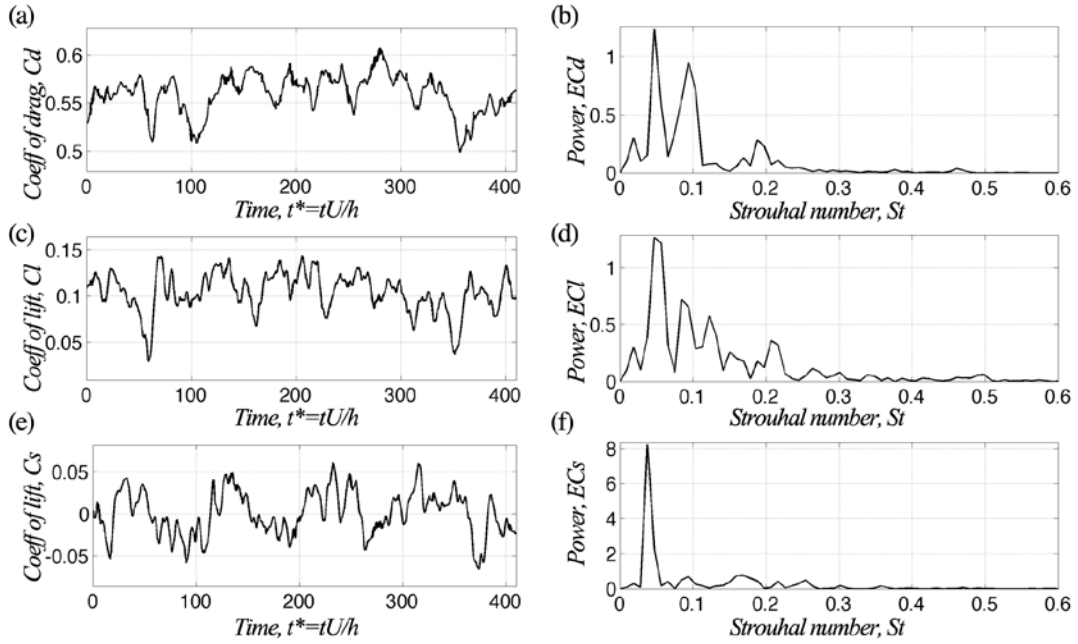
Fig. 21 Aerodynamic properties from the fine mesh (a) Time history of the coefficient of drag force. (b) Power spectral density of the coefficient of drag force. (c) Time history of the coefficient of lift force. (d) Power spectral density of the coefficient of lift force. (e) Time history of the coefficient of side force. (f) Power spectral density of the coefficient of side force.

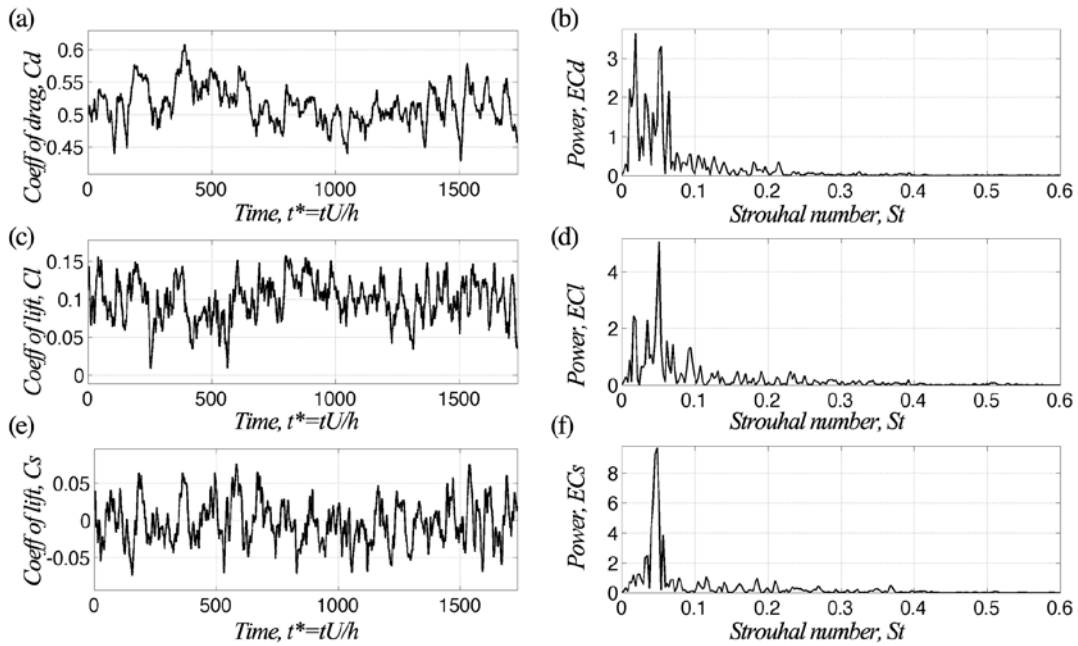Fig. 22 Aerodynamic properties from the coarse mesh (a) Time history of the coefficient of drag force. (b) Power spectral density of the coefficient of drag force. (c) Time history of the coefficient of lift force. (d) Power spectral density of the coefficient of lift force. (e) Time history of the coefficient of side force. (f) Power spectral density of the coefficient of side force.

8. Conclusions

1 A detailed investigation and visualisation of the flow structure around a 1/25th scale commercial
2 truck have been carried out based on LES results. Additional RANS simulations using different
3 turbulence models were also conducted. The surface pressure from both LES and RANS
4 simulations has been compared to full-scale experimental work and a reasonable level of
5 agreement was obtained only for the LES results. However, small discrepancies were found
6 near the front of the vehicle, which is believed to be due to the highly turbulent wind condition
7 in the full-scale tests. The Reynolds number difference between the full-scale and model-scale
8 may also contribute to the discrepancies, considering that region is relatively Reynolds number
9 sensitive. The time-averaged and time-dependent flow behaviours were examined. The
10 relationship between the aerodynamic forces and moments of the truck and the flow structures
11 generated around the vehicle were also studied. This investigation can draw the following
12 conclusions:

13   1. Detailed illustration of the complex flow structures around the truck subjected to headwinds
14   was obtained, which have not previously been identified.
15   2. Time-averaged surface trace lines and isosurface contour of pressure coefficient around the
16   truck show similar features found in a generic bluff body shape studied by Krajnović and
17   Davidson (2003). This demonstrates and further highlights that the investigation of flow
18   features around generic bluff bodies is of value. However, the difference due to detailed
19   features of the truck, especially the underbody, resulted in a noticeable change in the flow
20   behaviour compared to the generic cuboid shape, as indicated by the wake vortices.
21   3. Time-averaged vortex structures around the truck have been identified around and
22   underneath the vehicle showing regions of high turbulent activity, these locations are
23   associated with large energy losses. Instantaneous vortex structures were also investigated,
24   indicating the coherent vortex structures such as hairpin vortices and their propagation
25   along the surface of the truck.
26   4. Time-averaged pressure distribution along various cross-sectional lines at the truck surface
27   was examined and the pressure changes were linked to the flow structures.
28   5. A power spectral density analysis was carried out on the time histories of the aerodynamic
29   forces obtained from LES simulations to find out the dominant frequencies of vortex
30   shedding. For all the aerodynamic forces, two main instability modes were identified. One
31   mode corresponds to the large-scale vortex shedding in the wake of the vehicle that
32   periodically generates a wave motion. This low-frequency mode was identified at a
33   Strouhal number of 0.05 and represents the mean shedding frequency generated in the wake
34   of the vehicle. The other instability mode is called the spiral mode that generates small-
35   scale vortices in the shear layer due to the Kelvin Helmholtz instability. This corresponds
36   to the high-frequency components found in the power spectrums.

37 The details of this work will help engineers to better understand the problems faced with
38 producing lighter trucks and will allow them to make better-informed design modifications,
39 ultimately improving the fuel efficiency and safety of trucks.

40

References

Baker, C. J. 1991a. Ground Vehicles in High Cross Winds .1. Steady Aerodynamic Forces. *Journal of Fluids and Structures,* 5**,** 69-90.

Baker, C. J. 1991b. Ground Vehicles in High Cross Winds .2. Unsteady Aerodynamic Forces. *Journal of Fluids and Structures,* 5**,** 91-111.

Cheli, F., Belforte, P., Melzi, S., Sabbioni, E. & Tomasini, G. 2006. Numerical–experimental approach for evaluating cross-wind aerodynamic effects on heavy vehicles. *Vehicle System Dynamics,* 44**,** 791-804.

Cheli, F., Corradi, R., Sabbioni, E. & Tomasini, G. 2011. Wind tunnel tests on heavy road vehicles: Cross wind induced loads—Part 1. *Journal of Wind Engineering and Industrial Aerodynamics,* 99**,** 1000-1010.

Coleman, S. A. & Baker, C. J. 1990. High Sided Road Vehicles in Cross Winds. *Journal of Wind Engineering and Industrial Aerodynamics,* 36**,** 1383-1392.

Coleman, S. A. & Baker, C. J. 1994. An Experimental-Study of the Aerodynamic Behavior of High Sided Lorries in Cross Winds. *Journal of Wind Engineering and Industrial Aerodynamics,* 53**,** 401-429.

Department of Transport 2015. Transport Statistics Great Britain 2015. United Kingdom.

Diedrichs, B. 2010. Aerodynamic Crosswind Stability of a Regional Train Model. *Proceedings of the Institution of Mechanical Engineers, Part F: Journal of Rail and Rapid Transit,* 224**,** 580-591.

Duell, E. G. & George, A. R. 1999. Experimental Study of a Ground Vehicle Body Unsteady Near Wake. *SAE Transactions,* 108**,** 1589-1602.

Gallagher, M., Morden, J., Baker, C., Soper, D., Quinn, A., Hemida, H. & Sterling, M. 2018. Trains in crosswinds – Comparison of full-scale on-train measurements, physical model tests and CFD calculations. *Journal of Wind Engineering and Industrial Aerodynamics,* 175**,** 428-444.

Ghosal, S. & Moin, P. 1995. The Basic Equations for the Large Eddy Simulation of Turbulent Flows in Complex Geometry. *Journal of Computational Physics,* 118**,** 24-37.

Guilmineau, E., Deng, G. & Wackers, J. 2011. Numerical simulation with a DES approach for automotive flows. *Journal of Fluids and Structures,* 27**,** 807-816.

Hargreaves, D. & Morvan, H. 2007. Towards the validation of crosswind effects on a static high-sided vehicle. *NAFEMS International Journal of CFD Case Studies,* 7.

Hemida, H. & Baker, C. 2010. Large-eddy simulation of the flow around a freight wagon subjected to a crosswind. *Computers & Fluids,* 39**,** 1944-1956.

Hemida, H. & Krajnović, S. 2009. Transient Simulation of the Aerodynamic Response of a Double-Deck Bus in Gusty Winds. *Journal of Fluids Engineering-Transactions of the Asme,* 131.

Hemida, H. & Krajnović, S. 2010. LES study of the influence of the nose shape and yaw angles on flow structures around trains. *Journal of Wind Engineering and Industrial Aerodynamics,* 98**,** 34-46.

Hong, P., Marcu, B., Browand, F. & Tucker, A. 1998. Drag forces experienced by two, full-scale vehicles at close spacing. *California PATH Research Report.*

Hoxey, R. P., Kettlewell, P. J., Meehan, A. M., Baker, C. J. & Yang, X. 1996. An Investigation of the Aerodynamic and Ventilation Characteristics of Poultry Transport Vehicles: Part I, Full-scale Measurements. *Journal of Agricultural Engineering Research,* 65**,** 77- 83.

Hoxey, R. P., Richards, P. J. & Short, J. L. 2002. A 6 m cube in an atmospheric boundary layer flow Part 1. Full-scale and wind-tunnel results. *Wind and Structures,* 5**,** 165-176.

Hunt, J. C. R. 1988. Studying turbulence using direct numerical simulation: 1987 Center for Turbulence Research NASA Ames/Stanford Summer Programme. *Journal of Fluid Mechanics,* 190**,** 375-392.

Hyams, D. G., Sreenivas, K., Pankajakshan, R., Stephen Nichols, D., Roger Briley, W. & Whitfield, D. L. 2011. Computational simulation of model and full scale Class 8 trucks with drag reduction devices. *Computers & Fluids,* 41**,** 27-40.

Inagaki, M., Kondoh, T. & Nagano, Y. 2005. A mixed-time-scale SGS model with fixed model-parameters for practical LES. *Journal of Fluids Engineering-Transactions of the Asme,* 127**,** 1-13.

Issa, R. I. 1986. Solution of the implicitly discretised fluid flow equations by operator-splitting. *Journal of Computational Physics,* 62**,** 40-65.

Krajnović, S. 2009. Large eddy simulation of flows around ground vehicles and other bluff bodies. *Philosophical Transactions of the Royal Society a-Mathematical Physical and Engineering Sciences,* 367**,** 2917-2930.

Krajnović, S., Bengtsson, A. & Basara, B. 2011. Large Eddy Simulation Investigation of the Hysteresis Effects in the Flow Around an Oscillating Ground Vehicle. *Journal of Fluids Engineering-Transactions of the Asme,* 133.

Krajnović, S. & Davidson, L. 2002a. Large-eddy simulation of the flow around a bluff body. *Aiaa Journal,* 40**,** 927-936.

Krajnović, S. & Davidson, L. 2002b. A test case for large-eddy simulation in vehicle aerodynamics. *Engineering Turbulence Modelling and Experiments 5***,** 647-656.

Krajnović, S. & Davidson, L. 2003. Numerical study of the flow around a bus-shaped body. *Journal of Fluids Engineering-Transactions of the Asme,* 125**,** 500-509.

Krajnović, S. & Davidson, L. 2005a. Flow around a simplified car, Part 2: Understanding the flow. *Journal of Fluids Engineering-Transactions of the Asme,* 127**,** 919-928.

Krajnović, S. & Davidson, L. 2005b. Flow around, a simplified car, part 1: Large eddy simulation. *Journal of Fluids Engineering-Transactions of the Asme,* 127**,** 907-918.

Krajnović, S. & Fernandes, J. 2011. Numerical simulation of the flow around a simplified vehicle model with active flow control. *International Journal of Heat and Fluid Flow,* 32**,** 192-200.

1 Krajnović, S., Ringqvist, P., Nakade, K. & Basara, B. 2012. Large eddy simulation of the flow around a simplified
2   train moving through a crosswind flow. *Journal of Wind Engineering and Industrial Aerodynamics,* 110**,** 86-99.
3 Krajnović, S. A. & Davidson, L. 2003. Numerical study of the flow around a bus-shaped body. *Journal of Fluids
4   Engineering,* 125**,** 500-509.
5 Perry, A. E. & Chong, M. S. 1987. A description of eddying motions and flow patterns using critical point concepts.
6   *Annual Review of Fluid Mechanics,* 19**,** 125-155.
7 Quinn, A. D., Sterling, M., Robertson, A. P. & Baker, C. J. 2007. An investigation of the wind-induced rolling
8   moment on a commercial vehicle in the atmospheric boundary layer. *Proceedings of the Institution of
9   Mechanical Engineers, Part D: Journal of Automobile Engineering,* 221**,** 1367-1379.
10 Richards, P. J. & Quinn, A. D. 2002. A 6 m cube in an atmospheric boundary layer flow Part 2. Computational
11   solutions. *Wind and Structures,* 5**,** 177-192.
12 Smagorinsky, J. 1963. General circulation experiments with the primitive equations. *Monthly Weather Review, -* 91**,**
13   - 164.
14 Spalart, P. R. 2009. Detached-Eddy Simulation. *Annual Review of Fluid Mechanics,* 41**,** 181-202.
15 Sujudi, D. & Haimes 1995. Identification of swirling flow in 3-D vector fields. *AIAA, Paper No. AAIA 95-1715.*

16